# Direct nucleation of hexagonal boron nitride on diamond : crystalline properties of hBN nanowalls

# Accepted Manuscript

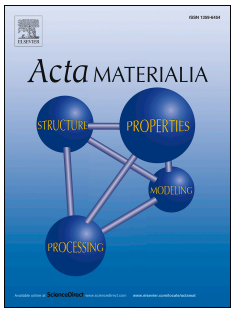


Direct nucleation of hexagonal boron nitride on diamond: Crystalline properties of hBN nanowalls

Duc-Quang Hoang, Svetlana Korneychuk, Kamatchi Jothiramalingam Sankaran, Paulius Pobedinskas, Sien Drijkoningen, Stuart Turner, Marlies K. Van Bael, Johan Verbeeck, Shannon S. Nicley, Ken Haenen

PII: S1359-6454(17)30003-4

DOI: 10.1016/j.actamat.2017.01.002

Reference: AM 13464

To appear in: *Acta Materialia*

Received Date: 30 August 2016

Revised Date: 3 January 2017

Accepted Date: 3 January 2017

Please cite this article as: D.-Q. Hoang, S. Korneychuk, K.J. Sankaran, P. Pobedinskas, S. Drijkoningen, S. Turner, M.K. Van Bael, J. Verbeeck, S.S. Nicley, K. Haenen, Direct nucleation of hexagonal boron nitride on diamond: Crystalline properties of hBN nanowalls, *Acta Materialia* (2017), doi: 10.1016/j.actamat.2017.01.002.

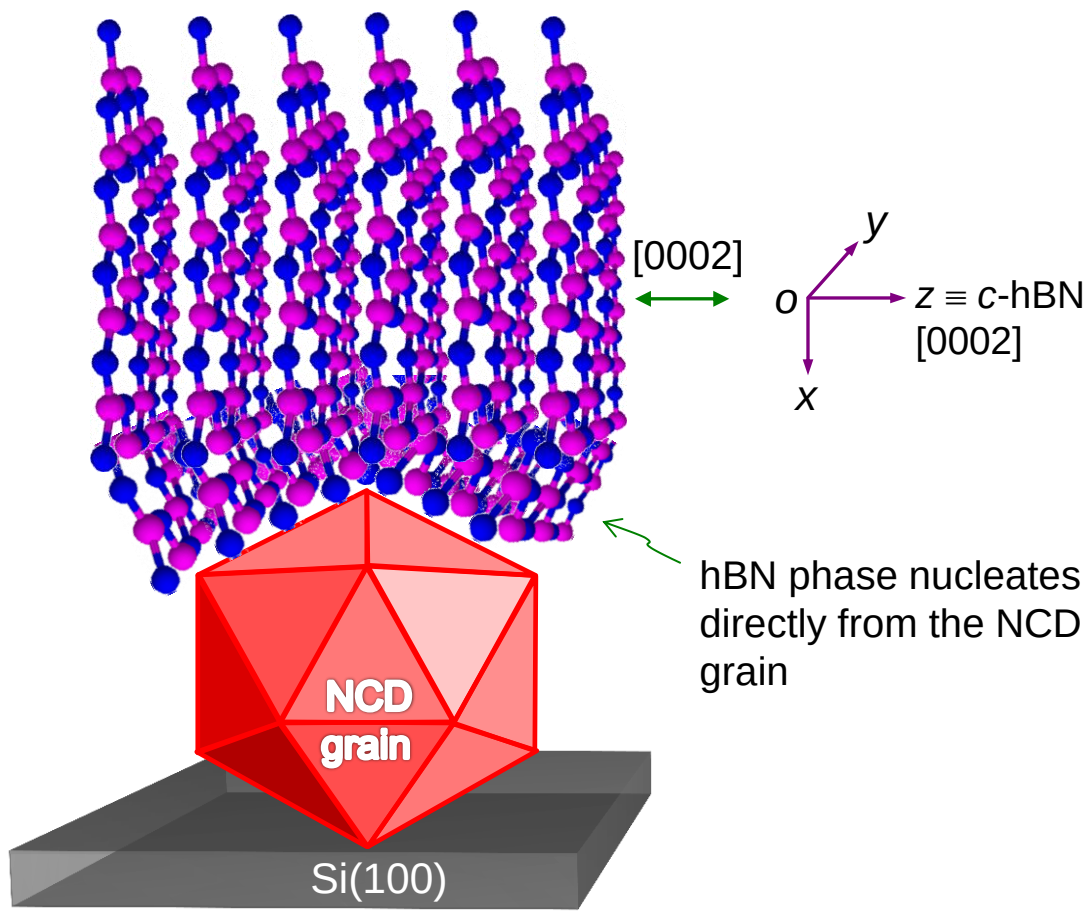
[0002]
y
o
z ≡ c-hBN
[0002]
x
hBN phase nucleates directly from the NCD grain
NCD grain
Si(100)

# Direct nucleation of hexagonal boron nitride on diamond: Crystalline properties of hBN nanowalls

Duc-Quang Hoang [a,b,*] , Svetlana Korneychuk [c], Kamatchi Jothiramalingam Sankaran [a,b], Paulius Pobedinskas [a,b], Sien Drijkoningen [a,b], Stuart Turner [c], Marlies K. Van Bael [a,b], Johan Verbeeck [c], Shannon S. Nicley [a,b], Ken Haenen [a,b,**]

[a]*Institute for Materials Research (IMO), Hasselt University, Diepenbeek, Belgium*

[b]*IMOMEC, IMEC vzw, Diepenbeek, Belgium*

[c]*Electron Microscopy for Materials Science (EMAT), University of Antwerp, Antwerp, Belgium*

E-mails: quang.hoang@uhasselt.be (D.-Q. Hoang) and ken.haenen@uhasselt.be (K. Haenen)

KEYWORDS: hexagonal boron nitride nanowalls, nanocrystalline diamond, heterostructures, physical vapor deposition.

**ABSTRACT**

Hexagonal boron nitride (hBN) nanowalls were deposited by unbalanced radio frequency sputtering system on (100)-oriented silicon, nanocrystalline diamond films, and amorphous silicon nitride ($Si_3N_4$) membranes. The hBN nanowall structures were found to grow vertically with respect to the surface of all of the substrates. To provide further insight into the nucleation phase and possible lattice distortion of the deposited films, the structural properties of the different interfaces were characterized by transmission electron microscopy.

For Si and $Si_3N_4$ substrates, turbostratic and amorphous BN phases form a clear transition zone between the substrate and the actual hBN phase of the bulk nanowalls. However, surprisingly, the presence of these phases was suppressed at the interface with a nanocrystalline diamond film, leading to a direct coupling of hBN with the diamond surface, independent of the vertical orientation of the diamond grain. To explain these observations, a growth mechanism is proposed in which the hydrogen terminated surface of the nanocrystalline diamond film leads to a rapid formation of the hBN phase during the initial stages of growth, contrary to the case of Si and $Si_3N_4$ substrates.

## 1. Introduction

Boron nitride (BN) materials have attracted much attention in recent years [1], due to a wide variety of promising future applications for coating and related technologies [2–5]. Hexagonal boron nitride (hBN) has a structure similar to graphite, in which B and N atoms are bound alternatively in in-plane hexagonal rings forming two dimensional (2D) sheets, which are held together by van der Waals forces, forming the hBN lattice. hBN can be synthesized into nanostructured films, such as nanowalls, with tunable properties depending on the growth parameters, to make it insulating, highly compressible, or to improve its lubricity [1, 5]. Grown hBN structures have so far shown a considerable number of defects and disordered BN phases, i.e. amorphous and turbostratic boron nitride (aBN and tBN), particularly at the initial stages of thin film growth. The presence of those phases is largely dependent on dynamics of chemical reactions at the substrate surface [1]. A substrate material that reduces these defective phases, creating a direct interface to the hBN phase, is therefore highly desirable.

Many excellent properties of diamond, such as a negative electron affinity on hydrogen terminated surfaces, mechanical hardness, chemical inertness, and good thermal conductivity

[6–9], make nanocrystalline diamond (NCD) thin films an interesting potential substrate material for hBN. For example, field electron emission devices that take advantage of the NEA of NCD thin films and the electric field enhancement factor of hBN nanowall structures, are an exciting potential application for these materials [10]. This work seeks to understand the nucleation and early growth phase of hBN layers on different substrates, including NCD films, by investigating the role of the different substrate surfaces on the crystallinity of the deposited hBN nanowalls at the BN-substrate interface.

## 2. Experimental details

### *2.1 Substrates*

Three types of substrates were used for hBN film growth – Si (100), NCD grown on Si (100), and amorphous $Si_3N_4$ membranes. 1×1 $cm^2$ Si (100) substrates were cut from a single side polished *n*-type Si wafer 500 – 550 μm in thickness, with a resistivity of 10–20 Ωcm, obtained from WAFERNET, INC. Si(100) substrates were cleaned using a standard cleaning procedure [11]. The 300 nm thick NCD layers were deposited on the same Si (100) substrates, with deposition conditions that will be given in Section 2.4. The membrane is a 35 nm-thick amorphous $Si_3N_4$ film supported on a 500 μm-thick silicon frame with a 100×100 $\mu m^2$ electron transparent window, obtained from TED PELLA, INC. The samples studied in this work are summarized in Table 1.

### *2.2 Deposition of the hBN films*

hBN thin films were synthesized in a home-built, unbalanced 13.56 MHz radio frequency (RF) sputtering system using optimized process conditions for nanowall formation, as determined in our previous work, i.e. a gas mixture of Ar(51%)/$N_2$(44%)/$H_2$(5%) and cathode power of 75 W [12]. A 3 inch diameter pyrolytic BN ceramic target (Kurt J. Lesker) with 99.99% material purity and a mass density of $1.96\times10^3$ $kg/m^3$ was used as the sputtering

target. The working pressure and target-to-substrate distance were fixed at $2.1 \times 10^{-2}$ mbar and 3 cm. The samples were unintentionally heated during the thin film deposition, due to reactive gas ion bombardment on the substrate surface [13]. The substrate temperature during growth was monitored through a thermocouple probe with a EUROTHERM 2408 controller, and was measured to be 125 °C for all of the depositions in this work.

### *2.3 Optical, morphological and TEM characterization*

Optical properties of the films were characterized by Raman spectroscopy with a HORIBA Jobin Yvon T64000 spectrometer using a blue laser (488 nm) in backscattering mode [14]. The Fourier transformed infrared (FTIR) transmission spectra of the films were taken at room temperature with a NICOLET$^{TM}$ 8700 spectrometer [15]. The FTIR measurements were performed normal to the film surface from 400–4000 $cm^{-1}$ with a resolution of 2.0 $cm^{-1}$, and the transmission spectrum of a bare Si (100) substrate was used as a baseline. Morphological properties of the films were investigated by electron microscopy using an FEI Quanta 200F field emission gun scanning electron microscope (FEG-SEM).

High resolution transmission electron microscopy (HRTEM) was performed on a JEOL 3000F microscope, equipped with a high-brightness Schottky-field emission electron source, and a high-resolution Gatan Imaging Filter (GIF2000) [16]. 80 kV accelerating voltages were used to minimize knock-on damage to the soft hBN material while retaining high contrast between the C, B, and N elements with similar atomic number (*Z*) [17]. 300 kV FEG accelerating operation voltages were used for annular dark field scanning TEM (ADF STEM) experiments, with the convergence and collection semi-angles in the range of 20 – 22 mrad. The TEM point resolution is 1.9 Å, and probe current and the energy spread are 0.5 nA and 1.2 eV, respectively.

*2.4 NCD film growth*

Si(100) substrates were seeded by spin-coating, using a $3.3 \times 10^{-4}$ kg/L water-based colloidal suspension of detonation nanodiamond particles with average size of 5-10 nm [18]. The NCD thin films were then grown by microwave plasma enhanced chemical vapor deposition (MWPECVD) in an ASTeX 6500 reactor, using a gas composition of 99% $H_2$ (396 sccm) / 1% $CH_4$ (4 sccm), a working pressure of 25 Torr, and a microwave power of 2500 W. The substrate temperature of 680 °C was constant for all the NCD growth runs and was monitored by single color optical pyrometry, assuming an optical emission coefficient $\epsilon = 0.3$. The film thickness was measured *in situ* during growth from the interference fringes of the reflection spectrum of a 405 nm diode-pumped solid state laser, and the deposition was stopped when the film thickness reached 300 nm. The resulting diamond film showed well-faceted grains, as seen in Fig. 1. These grains form as a result of the process of evolutionary selection of diamond, which assumes that a cubic diamond crystal consists out of the {001} and {111} faces. The growth of those grains occurs by propagation of these faces, of which depends on the ratio of the growth rates in the <001> and <111> directions, $v_{001}/v_{111}$. This parameter represents the ratio of the vertical distances of the {001} and {111} faces from the original nucleation point and can be controlled by the deposition parameters [19]. Wild *et al.* defined the well-known growth parameter, $\alpha = 3^{½}(v_{001}/v_{111})$ [20 – 22]. Therein, if $\alpha \geq 3$, the {001} planes disappear and the contour of a diamond grain is formed by four {111} faces, forming a pure octahedron, whilst if $\alpha \leq 1$, a cubic diamond crystallite is formed. For the cases of $\alpha$ between 1 and 3, all forms of cubo-octahedron facets can be produced [19, 22].

*2.5 TEM specimen preparation*

Samples were prepared for TEM analysis by thinning to electron transparency using either the gentle ion milling (IM) or focused ion beam (FIB) techniques [17, 23, 24], as given in

Table 1. For the IM technique, a sample is first cleaved into two halves that are glued face-to-face with an epoxy resin and then ground using a hand grinder to a thickness of ~120 μm. The glued slices were then continuously dimpled by a dimple grinder during ion polishing in a Balzers RES 010 precision ion polishing system, to a thickness of < 10 μm at the spherical indentation. The sample was then $Ar^+$ ion milled down to electron transparency of < 100 nm. $Ar^+$ ion energies of 1000 eV, 750 eV and 500 eV were used for 25 min each during the three step milling process on each side. An ion beam incidence angle of approximately 6° to 9° was used. The specimen was oscillated during the milling with an oscillation angle of ± 35°, to avoid back sputtering.

The FIB technique for sample thinning to electron transparency uses a FIB lift-out procedure, carried out in the FEI Helios NanoLab 650 FIB-SEM with a high-performance DualBeam system [23, 24]. The FIB consists of a gallium liquid metal ion source ($Ga^+$ LMIS) with an energy range of 5 keV to 30 keV, and a high resolution FEG-SEM. Thin layers of C and Pt were sputtered onto an area of interest on the sample with the electron and ion beam-induced depositions prior to FIB preparation to protect against re-deposition and/or contamination caused by the energetic $Ga^+$ ion beam during the lift-out procedure [24, 25]. The current profiles were varied from 10 pA to 20 nA during the FIB specimen preparation. During the final thinning and cleaning processes, the lowest ion beam current (10 pA) and energy (5 keV) were used on both sides of the specimen, with substrate tilting angles of ± 1° for thinning and ± 7° for cleaning from the 52° tilting of the ion beam. The final specimen thickness after the thinning and cleaning procedure is ~100 nm.

## 3. Results and Discussion

### *3.1 Interfacial crystalline properties: Hexagonal boron nitride on silicon and diamond*

To investigate the different surface morphologies of hBN grown on Si and NCD substrates, SEM analysis of samples T1 and T2 was performed, as shown in Fig. 2. The morphology of the NCD film prior the 300 nm-thick hBN film deposition is given in Fig. 2(c) for comparison. The hBN nanowalls appear bright in the SEM images, and are randomly oriented with respect to both the substrate surface and each other. While the hBN nanowalls grown on the Si substrate are spread equally on the substrate, appearing to form a homogeneous film, as shown in Fig. 2(a), the nanowalls grown on the NCD film (Fig. 2(b)) are clearly more localized to the facets of the NCD surface. Because the deposited BN film conformally coats the NCD substrate, the higher roughness of the NCD as compared to the smooth silicon surface causes a larger variation in wall-heights, and a perceived clustering of the nanowalls. The characteristics of the NCD film therefore have a large influence on the resulting hBN nanowall morphology, with the crystalline diamond grains appearing to form the preferential locations for the BN nanowalls to nucleate.

To further investigate a possible difference in the hBN nucleation mechanism on silicon and diamond, the growth rate ($R_G$) of hBN was determined via a series of experiments. Three pairs of hBN films were deposited at three fixed deposition times, $t_d$ = 66, 150 and 240 min, with the resulting film thickness *vs* $t_d$ plotted in Fig. 3. The thickness of the thin (D1) and medium (D2) films deposited on NCD are higher than that of the hBN films deposited on silicon (Si1 and Si2) for the same $t_d$, indicating a larger $R_G$ on diamond. This implies a difference in the nucleation and/or initial stage of thin film growth. Looking more in detail to Fig. 3, the thickness of hBN-on-Si clearly increases quasi-linearly with deposition time. By contrast, when using NCD substrates, the growth speed tends to be slower for longer deposition times (Table 1). It is argued that the subsequent growth of hBN on the NCD facets is complicated by the clustering of the nanowalls on the diamond crystal facets and the inherent larger roughness of NCD, as discussed earlier. BN films deposited on the smooth

silicon substrates do not have these limitations, and the thickness continues to increase quasi-linearly.

To investigate the difference in the crystalline quality at the interface of hBN with Si and NCD substrates, samples T1 and T2 were characterized by bright field (BF) HR TEM and ADF STEM, as shown in Fig. 4. A significant difference can be seen in the BN crystallinity close to the Si surface compared to the NCD surface. A mixture of hBN, tBN and aBN phases is observed for the region in contact with the Si surface [26], as seen in Fig. 4(a). The aBN and tBN phases in particular are much more prevalent at the Si/BN interface than in the same region of the NCD/BN structure. The mixed phase of aBN and tBN extend a few tens of nanometers from the Si substrate surface before the hBN nanowall structures become more dominant [27]. The quality of the deposited BN films on the Si substrate, especially at the initial stage of thin film growth, is therefore largely dependent on many other deposition factors, i.e. target-to-substrate distance ($d$), substrate tilting angle ($\alpha$), substrate temperature ($T_{sub}$), ambient mixed gases, and RF power [12, 27], which determine the conditions for the nucleation of the hBN phase remote from the surface.

The aBN and tBN phases at the interface of the Si/BN film thus result from chemical and physical processes at the initial stage of the thin film growth [28]. If the sputtered ions do not initially form chemical bonds to substrate nucleation sites or to BN material already present, they can migrate across the substrate surface until stable positions are found, which may not cause them to incorporate in an ordered lattice structure [28]. In this case aBN material is formed, as seen at the initial stage of thin film growth on the Si surface. Remarkably, when looking at the interface between BN and diamond, the aBN/tBN phases are completely absent, with clear crystalline hexagonal boron nitride phase directly connected to the underlying diamond grain. As seen in Fig. 1 and Fig. 2(c), the NCD film shows well faceted

grains without a clear preferred orientation that might develop for thicker films [29]. The specific orientation of the different grains does not seem to play a role in the direct nucleation of the hBN on the diamond surface, nor on the eventual orientation of the hBN nanowalls. The hBN nanosheets, indicated as cyan dashed-arrows in Fig. 4(b), eventually grow perpendicular to the overall substrate surface, i.e. parallel to the incoming ion flux from the target to the substrate (indicated as a green arrow) irrespective of the local facet orientation (denoted as yellow and purple dashed-lines).

### *3.2 Nanowall crystalline properties*

#### *3.2.1 hBN on $Si_3N_4$ membranes*

In order to gain a better understanding of the overall crystallinity of the nanowalls and their spatial in-plane distribution, an investigation of a thin hBN film by HR TEM parallel to the growth direction was undertaken. A 35 nm thick $Si_3N_4$ membrane was used as the substrate, on which 100 nm of BN was deposited, keeping the combined structure electron transparent and thus avoiding additional processing steps before the TEM investigation.

Figure 5(a) shows a bright field (BF) TEM image of the T3 specimen, and its electron diffraction (ED) pattern is shown in the inset. The hBN nanowalls are thicker than the surrounding material, and therefore appear dark in the image. The nanowalls are randomly oriented in the plane parallel to the $Si_3N_4$ membrane surface and they show variation in the heights and widths of the walls. As already shown by SEM in Fig. 2(a), the walls are oriented vertical to the substrate surface, as also evidenced by the ED pattern shown in the inset of Fig. 5(a). The electron intensity of the (0002) ring is homogeneous and continuous, indicating that the [0002] directions of the deposited hBN nanowalls are randomly oriented parallel to the substrate surface (vertical to the transmitted electron beam direction). The size distribution of the nanowalls was quantified through image analysis by modeling the

nanowalls as ellipses, as shown in Fig. 5(b). The narrow peak of the wall-width distribution confirms that the specimen shows good homogeneity of nanowalls. (See also Fig. S1 and the accompanying explanation on the determination of the size distribution in the Supplementary Data (SD))

Studying the area in Fig. 5(a) in more detail, two different kinds of morphologies can be identified, one with well-defined ellipsoidal nanowalls, and the spaces in between with more complicated nanowall structures. To further investigate the crystallinity of individual hBN nanowalls in those regions, higher magnification BF HRTEM images were taken. Fig. 5(c) shows the image corresponding to an area where the nanowalls have simple geometries that are well described as ellipses. This is illustrated by the dashed ellipse that nicely borders an individual nanowall. Based on an electron intensity profile taken across the line AB, as given in the inset of Fig. 5(c) and also described in the SD, the nanowall height is inhomogeneous within the wall, with a high central part that gradually decreases in height towards the outsides of the wall. The HRTEM image of a region with more complicated nanowall geometries (Fig. 5(d)) shows a greater degree of overlap between neighboring walls. Both regions show the presence of wrinkles, as denoted by green arrows in Figs. 5(c) and (d). This wrinkling behavior can result from stress or strain caused by defects during the material growth [27, 30].

### *3.2.2 Hexagonal boron nitride on silicon and diamond*

To further assess the crystalline properties, samples T1 and T2 were characterized by Raman and FTIR spectroscopy (Fig. 6). The width of the Raman frequency ($E_{2g}$ at 1368 $cm^{-1}$) mode of the $sp^2$ hBN material can be used to determine the quality of the pure hBN phase [1, 5, 31]. In Figs. 6(a) and (b), these peaks are shown for the two samples studied. While the full-width at half maximum ($\Gamma_{½}$) value of the $E_{2g}$ peak was measured to be ~26 $cm^{-1}$ for sample T1, a

much lower value of ~18 $cm^{-1}$ could be determined for T2, indicating that the hBN crystalline quality in the latter sample is higher. This confirms the HRTEM observations presented in Fig. 4, where hBN was directly deposited on the diamond surface without the presence of an aBN/tBN interface. The Raman spectrum of sample T2 also shows characteristics of the diamond film, with the first order Raman mode peaks of diamond ($sp^3$) at 1333 $cm^{-1}$ and non-diamond carbon ($sp^2$) present in the grain boundaries at 1489 $cm^{-1}$ [32].

FTIR was used to detect the vibrational modes of the most common defects in hBN the samples, such as N-H (3437 $cm^{-1}$) [27, 33], B-C (1100 $cm^{-1}$) [34, 35], and $sp^3$ BN (1085–1110 $cm^{-1}$) [36, 37]. The N-H absorption peak intensity is related to defects in the hBN lattice as described in our previous work [27]. The infrared absorption spectra for samples T1 and T2 are shown in Figs. 6(c) and (d). The features seen at 1110 $cm^{-1}$ (indicated by the dashed arrows) could be due to the presence of $sp^3$ BN or B-C. Although $sp^3$ BN is not expected to form at the substrate temperature (125 °C) and the cathode power (75 W) investigated in this work, some $sp^3$ bonding could be present in the disordered BN phase in between the nanowalls [36]. However, it is more likely that the 1110 $cm^{-1}$ feature originates from the B-C mode due to already observed contamination with carbon, and in the case of T2, partly due the possible presence of B-C bonds at the diamond-BN interface [12, 35]. Both spectra of course also show the expected B-N bending ($A_{2u}$ at 817 $cm^{-1}$) and B-N stretching ($E_{1u}$ at 1376 $cm^{-1}$) optical phonon modes of the $sp^2$ hBN [1, 5, 31].

### *3.2.3 Hexagonal boron nitride on diamond: Nucleation model*

In earlier work by Hoang *et al.* carried out on silicon substrates, it was proven that the hBN formation is primarily a chemically driven process rather than a physical one, leading to nanowalls that are vertically oriented with respect to the substrate surface, irrespective of the relative substrate-target orientation [27]. As supported by the electron diffraction pattern of

Fig. 5(a), this is also the case when a $Si_3N_4$ membrane is used as a substrate. As discussed above, the interface between the deposited BN film and the NCD surface shows virtually no presence of disordered BN phases. The hBN phase seems to nucleate directly onto the diamond surface. Despite the fact that the different diamond facets are clearly not all parallel to the Si substrate surface, vertically oriented nanowalls are still observed, indicating that after nucleation, the hBN nanowalls change their orientation slightly during the first stages of growth, as seen in Fig. 4(b). This hints strongly at some influence of the direction of the incoming ion flux, i.e. a physical effect. Nevertheless, the question remains as to what underlying process drives the direct nucleation of hBN on diamond. To obtain hBN nanowalls, the addition of hydrogen to the process gas is a prerequisite [12]. The NCD films are used are as-grown, i.e. they are H-terminated when taken out of the diamond plasma deposition reactor. Here, it is proposed that the combination of a hydrogen terminated diamond surface and the abundance of hydrogen during the BN deposition process play a crucial role in the observed hBN crystalline phase at the interface with the diamond substrate. As a notice, an amorphous carbon film with dangling bonds or hydrogen termination surface does not create the same effect as an NCD surface. Dangling bonds of the amorphous carbon surface are randomly oriented or easily saturated in energy at the surface due to their cross-linkages, making it difficult for them to connect with B or N ions present in the deposition chamber. The hydrogen termination of the NCD surface is a result of the diamond deposition process and prevents cross-linking, while stabilizing the $sp^3$ nature of the carbon bonds during diamond growth. The H-termination appearing on the NCD surface thus plays two key roles: (1) keeps the $sp^3$ diamond lattice stable; (2) during hBN growth, some of these H atoms will be removed by reactive gas ion bombardment in the RF sputtering chamber and replaced by B or N species afterwards, as described schematically in Fig. 7.

The proposed growth model begins with the abstraction of an H atom terminating the surface of the diamond substrate by a sputtered B ion [34, 39], which nucleates the hBN ring, as seen in Figs. 7(b) and (c). Two sputtered N ions can then react with the B-site to form one-third of the hBN ring with two N terminated edges, as shown in Figs. 7(c–e). Two other sputtered B-ions then join the resulting N-sites, and this process proceeds one more time, ending with an N locking the last two B-sites into the first ring in the nucleated hBN lattice, as shown in Fig. 7(f). The hBN nanosheet formation then proceeds from this initial template. The hBN nanosheet therefore orients vertically to the substrate surface due to the locked orientation of the first atom in this nucleation ring, resulting from the surface H abstraction site. Consequently, the H-termination of the NCD surface is key to the formation of the hBN nanowall structures via the process outlined in Fig. 7.

## 4. Conclusions

The deposition of hexagonal boron nitride nanowalls achieved by unbalanced RF sputtering was investigated. HRTEM characterization showed that the disordered BN phases that formed at the interface with Si substrates were significantly reduced in the case of diamond substrates, where a rapid formation of the crystalline hBN phase at the initial stage of thin film growth was observed. It is proposed that the presence of hydrogen at the diamond surface plays an important role in allowing the hexagonal BN phase to nucleate directly from the diamond surface without prior aBN/tBN formation. These results are further supported through Raman and FTIR spectroscopy data, showing that the hBN crystallinity was higher for hBN on NCD than as compared to hBN on Si. The achieved reduction of disordered BN phases at the BN-diamond interface, increasing the crystalline quality of the hBN nanowalls presents substantial progress toward the realization of hBN nanowalls applications that require high crystalline quality and interfacial properties.

**Acknowledgements**

The authors want to thank Mr. J. Baccus, Mr. B. Ruttens and Prof. Jan D'Haen for technical and experimental assistance, and Prof. Hans-Gerhard Boyen and Dr. Duc-The Ngo (The University of Manchester) for fruitful discussions. KJS, PP and ST are Postdoctoral Fellows of the Research Foundation - Flanders (FWO). The Hercules Foundation Flanders is acknowledged for financial support of the Raman equipment.

**Appendix A: Supplementary data**: Supplementary data related to this article can be found at http://dx.doi.org/10.1016/**********.

**References**

[1] A. Pakdel, Y. Bando, D. Golberg, Nano boron nitride flatland, Chem. Soc. Rev. 43 (2014) 934–959.

[2] K. Watanabe, T. Taniguchi, T. Niiyama, K. Miya, M. Taniguchi, Far-ultraviolet plane-emission handheld device based on hexagonal boron nitride, Nat. Photon. 3 (2009) 591–594.

[3] K.H. Lee, H.J. Shin, J. Lee, I.Y. Lee, G.H. Kim, J.Y. Choi, S.W. Kim, Large-scale synthesis of high-quality hexagonal boron nitride nanosheets for large-area graphene electronics, Nano Lett. 12 (2012) 714–718.

[4] W. Lei, V.N. Mochalin, D. Liu, S. Qin, Y. Gogotsi, Y. Chen, Boron nitride colloidal solutions, ultralight aerogels and freestanding membranes through one step exfoliation and functionalization, Nat. Commun. 6 (2015) 8849–8856.

[5] Y. Lin, J.W. Connell, Advances in 2D boron nitride nanostructures: Nanosheets, nanoribbons, nanomeshes, and hybrids with graphene, Nanoscale 4 (2012) 6908–6939.

[6] J.E. Butler, A.V. Sumant, The CVD of nanodiamond materials, Chem. Vap. Deposition 14 (2008) 145–160.

[7] R.J. Nemanich, J.A. Carlisle, A. Hirata, K. Haenen, CVD diamond - research, applications, and challenges, MRS Bull. 39 (2014) 490–494.

[8] Y. Takano, Superconductivity in CVD diamond films, J. Phys.: Condens. Matter 21 (2009) 253201–253211.

[9] O.A. Shenderova, G.E. McGuire, Science and engineering of nanodiamond particle surfaces for biological applications, Biointerphases 10 (2015) 030802–030823.

[10] K.J. Sankaran, D.Q. Hoang, S. Kunuku, S. Korneychuk, S. Turner, P. Pobedinskas, S. Drijkoningen, M.K. Van Bael, J. D'Haen, J. Verbeeck, K.C. Leou, I.N. Lin, K. Haenen, Enhanced optoelectronic performances of vertically aligned hexagonal boron nitride nanowalls nanocrystalline diamond heterostructures, Sci. Rep. 16 (2016) 29444–29454.

[11] W. Kern, D.A. Puotinen, Cleaning solutions based on hydrogen peroxide for use in silicon semiconductor technology, RCA Rev. 31 (1970) 187–205.

[12] B. BenMoussa, J. D'Haen, C. Borschel, J. Barjon, A. Soltani, V. Mortet, C. Ronning, M. D'Olieslaeger, H.-G. Boyen, K. Haenen, Hexagonal boron nitride nanowalls: Physical vapour deposition, 2D/3D morphology and spectroscopic analysis, J. Phys. D: Appl. Phys. 45 (2012) 135302–135311.

[13] K. Strijckmans, W.P. Leroy, R. De Gryse, D. Depla, Modeling reactive magnetron sputtering: Fixing the parameter set, Surf. Coat. Tech. 206 (2012) 3666–3675.

[14] P. Pobedinskas, G. Gegutis, W. Dexters, A. Hardy, M.K. Van Bael, K. Haenen, Influence of hydrogen and hydrogen/methane plasmas on AlN thin films, Appl. Phys. Lett. 104 (2014) 081917–081920.

[15] P. Pobedinskas, B. Ruttens, J. D'Haen, K. Haenen, Optical phonon lifetimes in sputtered AlN thin films, Appl. Phys. Lett. 100 (2012) 191906–191909.

[16] S. Heyer, W. Janssen, S. Turner, Y.-G. Lu, W.S. Yeap, J. Verbeeck, K. Haenen, A. Krueger, Toward deep blue nano hope diamonds: Heavily boron-doped diamond nanoparticles, ACS Nano 8 (2014) 5757–5764.

[17] D.B. Williams, C.B. Carter, Transmission Electron Microscopy: A Textbook for Materials Science, Springer Science, LLC 1996, 2009.

[18] O.A. Williams, O. Douhéret, M. Daenen, K. Haenen, E. Osawa, M. Takahashi, Enhanced diamond nucleation on monodispersed nanocrystalline diamond, Chem. Phys. Lett. 445 (2007) 255–258.

[19] Christoph E. Nebel and Juergen Ristein (eds) (2003), "*Thin-Film Diamond I*", *Semiconductors and Semimetals*, Vol. 76, Elsevier Academic Press, 33–36.

[20] C. Wild, P. Koidl, W. Müller-Sebert, H. Walcher, R. Kohl, N. Herres, R. Locher, R. Samlenski, R. Brenn, Chemical vapour deposition and characterization of smooth {100}-faceted diamond films, Diamond Relat. Mater. 2 (1993) 158–168.

[21] Ch. Wild, N. Herres, P. Koidl, Texture formation in polycrystalline diamond films, J. Appl. Phys. 68 (1990) 973–978.

[22] P. Smereka, X.-Q Li, G. Russo, D.J. Srolovitz, Simulation of faceted film growth in three dimensions: microstructure, morphology and texture, Acta Mater. 53 (2005) 1191–1204

[23] S. Turner, Y.G. Lu, S.D. Janssens, F.D. Pieve, D. Lamoen, J. Verbeeck, K. Haenen, P. Wagner, G.V. Tendeloo, Local boron environment in B-doped nanocrystalline diamond films, Nanoscale 4 (2012) 5960–5964.

[24] J. Mayer, L.A. Giannuzzi, T. Kamino, J. Michael, TEM sample preparation and FIB-induced damage, MRS Bull. 32 (2007) 400–407.

[25] A.V. Krasheninnikov, K. Nordlund, Ion and electron irradiation-induced effects in nanostructured materials, J. Appl. Phys. 107 (2010) 071301–071370.

[26] P.B. Mirkarimi, K.F. McCarty, D.L. Medlin, Review of advances in cubic boron nitride film synthesis, Mater. Sci. Eng. R-Rep. 21 (1997) 47–100.

[27] D.Q. Hoang, P. Pobedinskas, S.S. Nicley, S. Turner, S.D. Janssens, M.K. Van Bael, J. D'Haen, K. Haenen, Elucidation of the growth mechanism of sputtered 2D hexagonal boron nitride nanowalls, Cryst. Growth Des. 16 (2016) 3699–3708.

[28] C.T. Rettner, D.J. Auerbach, J.C. Tully, A.W. Kleyn, Chemical dynamics at the gas-surface interface, J. Phys. Chem. 100 (1996) 13021–13033.

[29] O.A. Williams, M. Nesladek, M. Daenen, S. Michaelson, A. Hoffman, E. Osawa, K. Haenen, R.B. Jackman, Growth, electronic properties and applications of nanodiamond, Diamond Relat. Mater. 17 (2008) 1080–1088.

[30] A.L. Gibb, N. Alem, J.H. Chen, K.J. Erickson, J. Ciston, A. Gautam, M. Linck, A. Zettl, Atomic resolution imaging of grain boundary defects in monolayer chemical vapor deposition-grown hexagonal boron nitride, J. Am. Chem. Soc. 135 (2013) 6758–6761.

[31] R.J. Nemanich, S.A. Solin, R.M. Martin, Light scattering study of boron nitride microcrystals, Phys. Rev. B 23 (1981) 6348–6356.

[32] V. Mortet, L. Zhang, M. Eckert, J. D'Haen, A. Soltani, M. Moreau, D. Troadec, E. Neyts, J.C. De Jaeger, J. Verbeeck, A. Bogaerts, G. Van Tendeloo, K. Haenen, P. Wagner, Grain size tuning of nanocrystalline chemical vapor deposited diamond by continuous electrical bias growth: Experimental and theoretical study, Phys. Status Solidi A 209 (2012) 1675–1682.

[33] W.A. Lanford, M.J. Rand, The hydrogen content of plasma deposited silicon nitride, J. Appl. Phys. 49 (1978) 2473–2477.

[34] E. Pascual, E. Martínez, J. Esteve, A. Lousa, Boron carbide thin films deposited by tuned-substrate RF magnetron sputtering, Diamond Relat. Mater. 8 (1999) 402–405.

[35] Y. Wada, Y.K. Yap, M. Yoshimura, Y. Mori, T. Sasaki, The control of B-N and B-C bonds in BCN films synthesized using pulsed laser deposition, Diamond Relat. Mater. 9 (2000) 620–624.

[36] S.Y. Shapoval, V.T. Petrashov, O.A. Popov, A.O. Westner, M.D. Yoder Jr., C.K.C. Lok, Cubic boron nitride films deposited by electron cyclotron resonance plasma, Appl. Phys. Lett. 57 (1990) 1885–1886.

[37] H. Feldermann, R. Merk, H. Hofsäss, C. Ronning, T. Zheleva, Room temperature growth of cubic boron nitride, Appl. Phys. Lett. 74 (1999) 1552–1554.

[38] P.W. May, Diamond thin films: a 21st-century material, Phil. Trans. R. Soc. Lond. A 358 (2000) 473–495.

[39] J.E. Butler, I. Oleynik, A mechanism for crystal twinning in the growth of diamond by chemical vapour deposition, Phil. Trans. R. Soc. A 366 (2008) 295–311

**Table 1** Samples studied in this work. TEM preparation methods for the purpose of thinning the samples to electron transparency refer to: gentle ion milling (IM) encapsulation and focused ion beam (FIB) techniques. T3 was only grown to a thickness of 100 nm thus remained electron transparent.

| Sample name | Substrate | hBN thickness (nm) | TEM preparation method | Deposition time ($t_d$) (min) | Average growth rate ($R_G$) (nm/h) |
|---|---|---|---|---|---|
| T1 | Si (100) | 300 ± 18 | IM | 79 | 228 ± 18 |
| T2 | NCD | 300 ± 25 | FIB | 54 | 333 ± 25 |
| T3 | a-$Si_3N_4$ membrane | 100 ± 18 | - | 26 | 231 ± 18 |
| Si1 | Si (100) | 250 ± 16 | - | 66 | 228 ± 16 |
| D1 | NCD | 370 ± 27 | - | 66 | 336 ± 27 |
| Si2 | Si (100) | 700 ± 33 | - | 150 | 280 ± 33 |
| D2 | NCD | 800 ± 39 | - | 150 | 320 ± 39 |
| Si3 | Si (100) | 1080 ± 38 | - | 240 | 270 ± 38 |
| D3 | NCD | 970 ± 41 | - | 240 | 242 ± 41 |

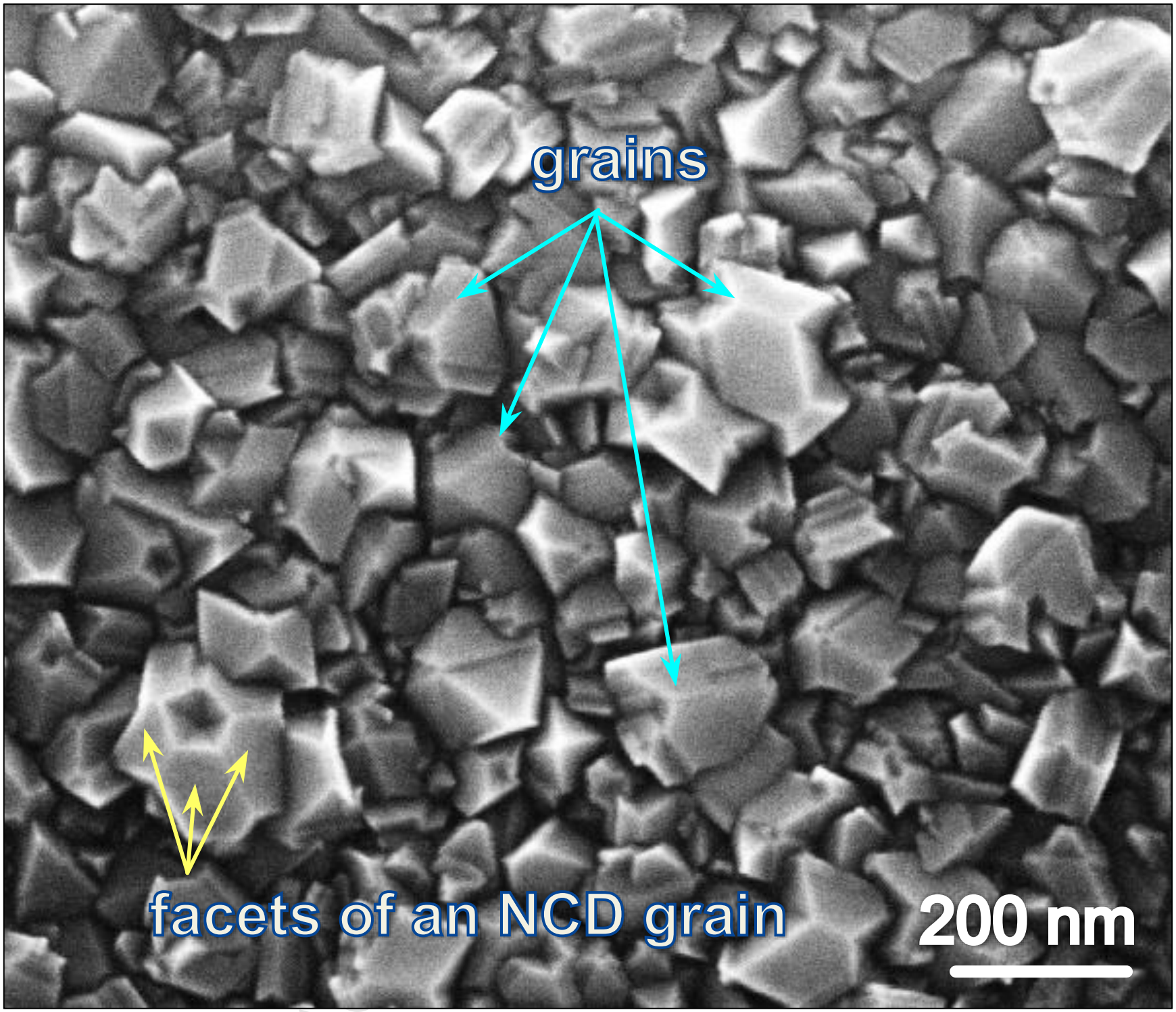


**Figure 1** SEM image of the 300 nm-thick NCD film grown on a Si(100) substrate showing well-faceted grains.

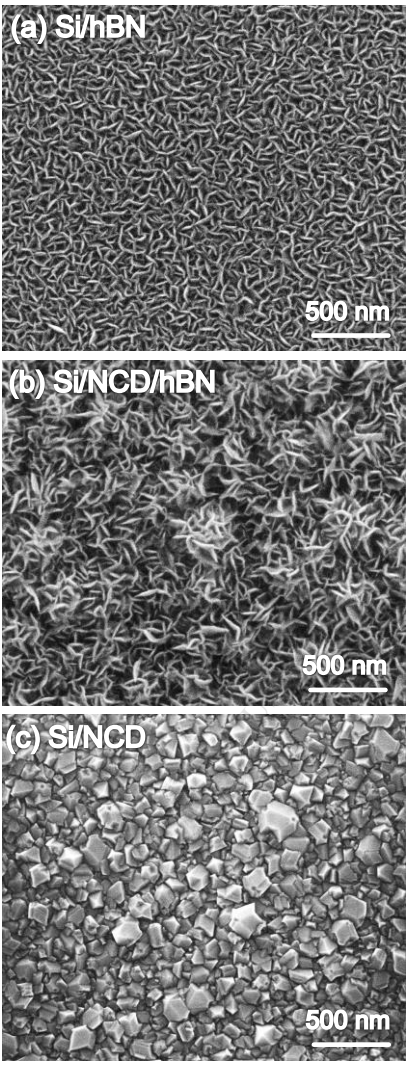


**Figure 2** SEM images of (a) sample T1, a 300 nm-thick hBN nanowall film deposited on a Si(100) substrate (b) T2, a 300 nm-thick hBN nanowall film deposited on a NCD film (c) the 300 nm-thick NCD film prior to the hBN deposition.

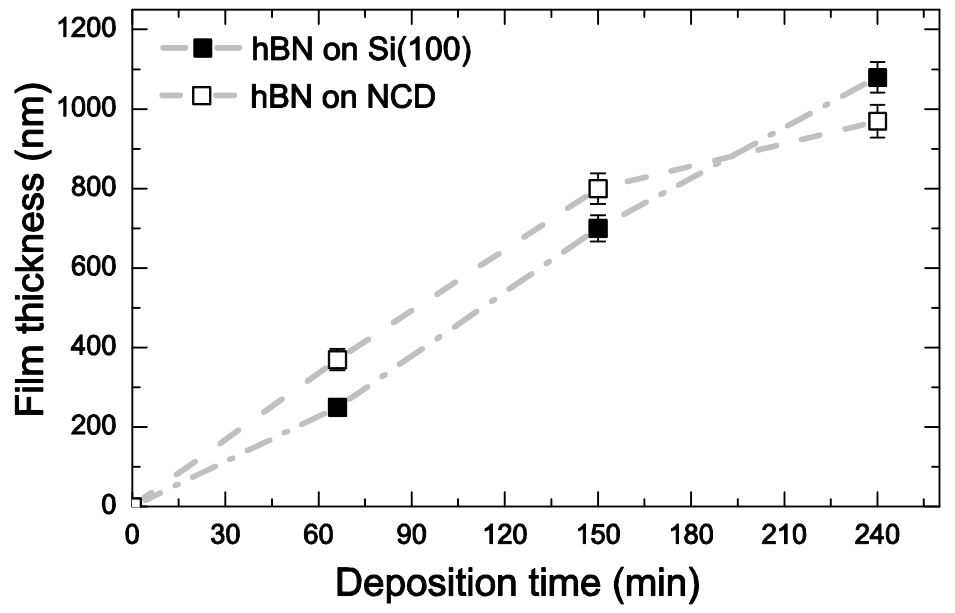


**Figure 3** Thicknesses of hBN films deposited on Si (100) and NCD substrates as a function of deposition times. Each point represents a single deposition with error bars computed independently for each film, as the standard deviation for the measurement of 10 different points in the cross-sectional SEM images used for thickness determination.

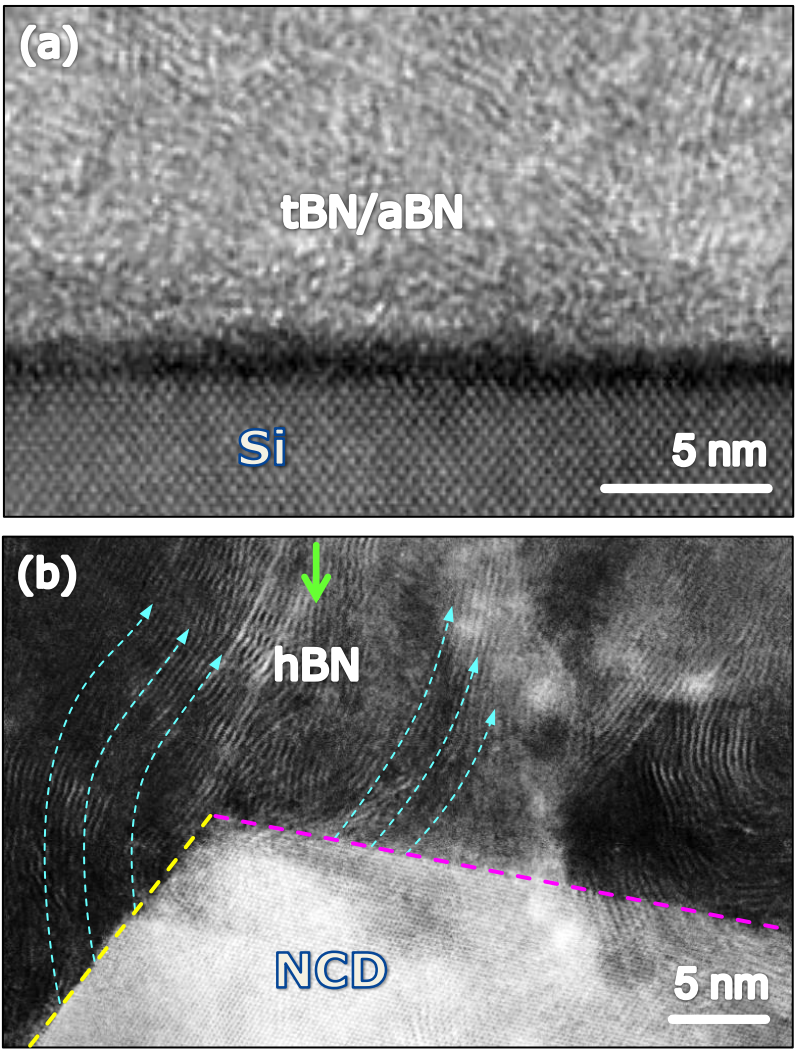


**Figure 4** (a) A HR TEM image of the interface between the Si substrate and BN material showing turbostratic and amorphous BN phases. (b) ADF STEM image of the interface of the NCD substrate and hBN film, showing high crystallinity and the presence of the hBN phase starting directly at the interface with diamond. Cyan dashed-arrows indicate typical hBN nanosheets that nucleate and grow directly from the facets of the NCD grain.

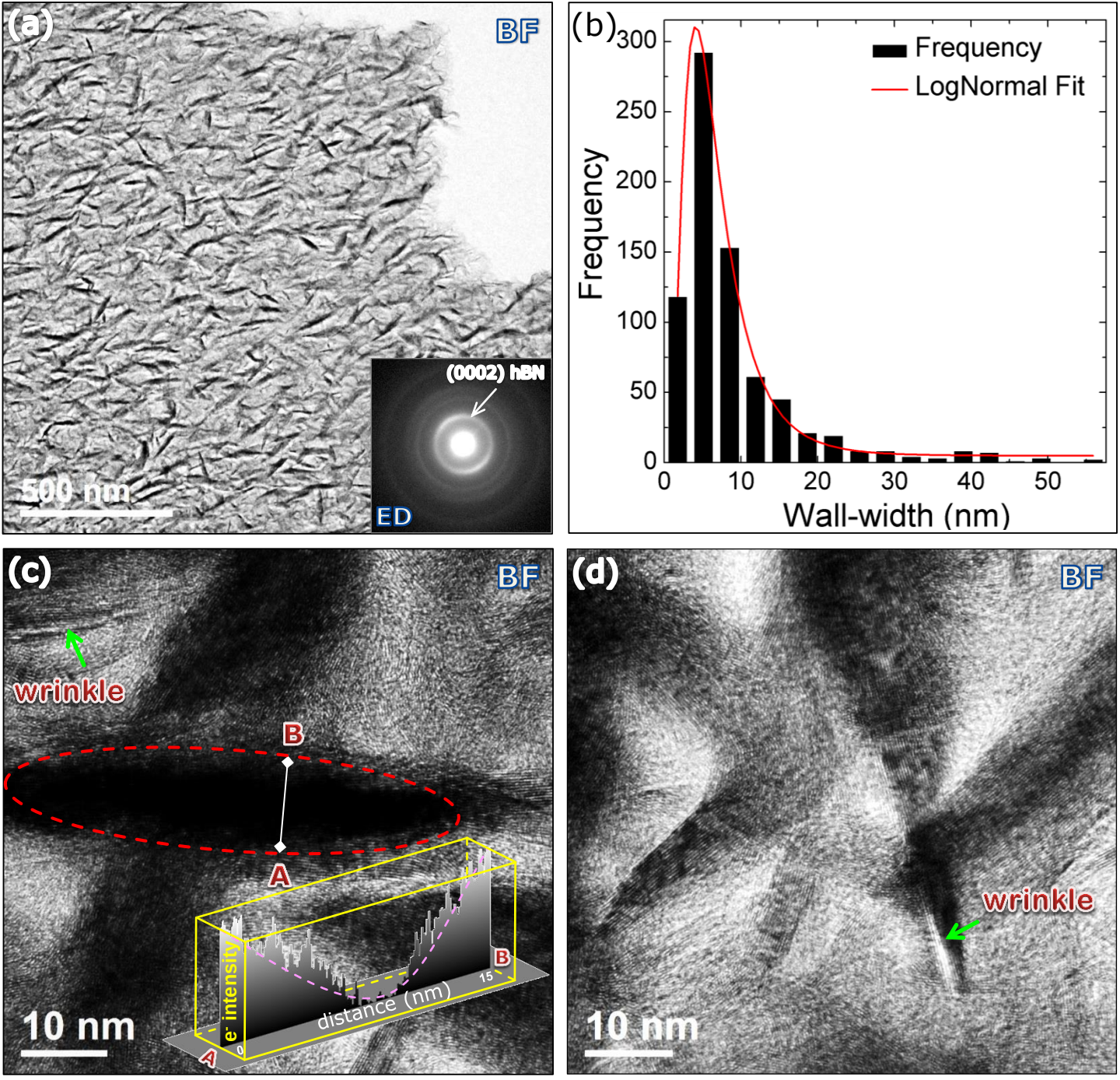


**Figure 5** (a) A BF TEM image of a 100 nm-thick hBN film deposited on a $Si_3N_4$ membrane (sample T3). The inset is an ED pattern taken in the same region. (b) The width distribution of the walls determined from (a) (see text). (c) and (d) BF HRTEM images recorded from two representative areas from the area shown in (a), with well-defined (c) and more defective (d) nanowall profiles. The inset in (c) is an electron intensity profile that was extracted from A to B connecting two sides of the nanowall circled in the dashed ellipse.

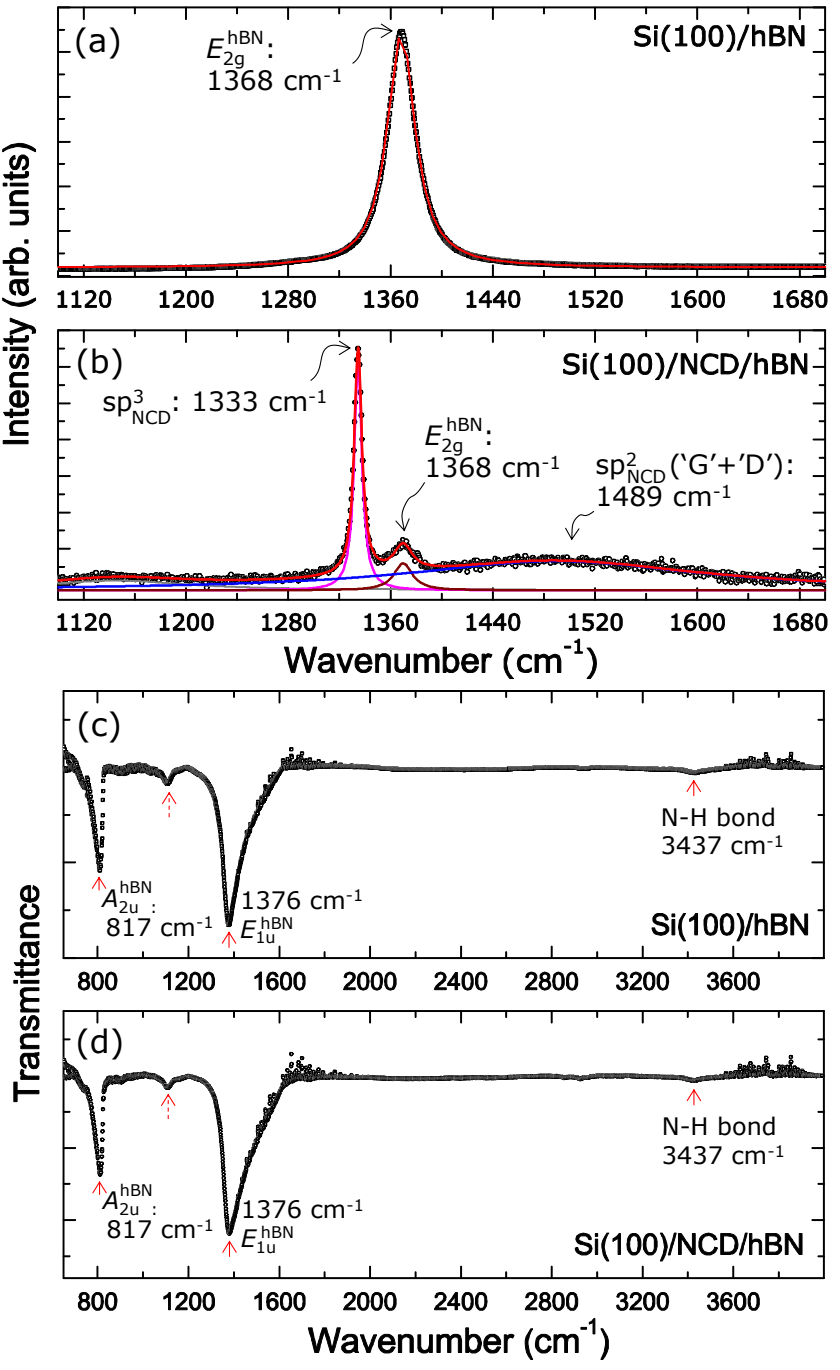


**Figure 6** (a) Raman spectrum for sample T1 (b) Raman spectrum for sample T2 (c) FTIR transmittance spectrum for sample T1 (d) FTIR transmittance spectrum for sample T2. The red solid lines showing in (a) and (b) are the best fits for those Raman spectra. The other colored lines in (b) are three different characteristic peaks associated diamond and hBN films.

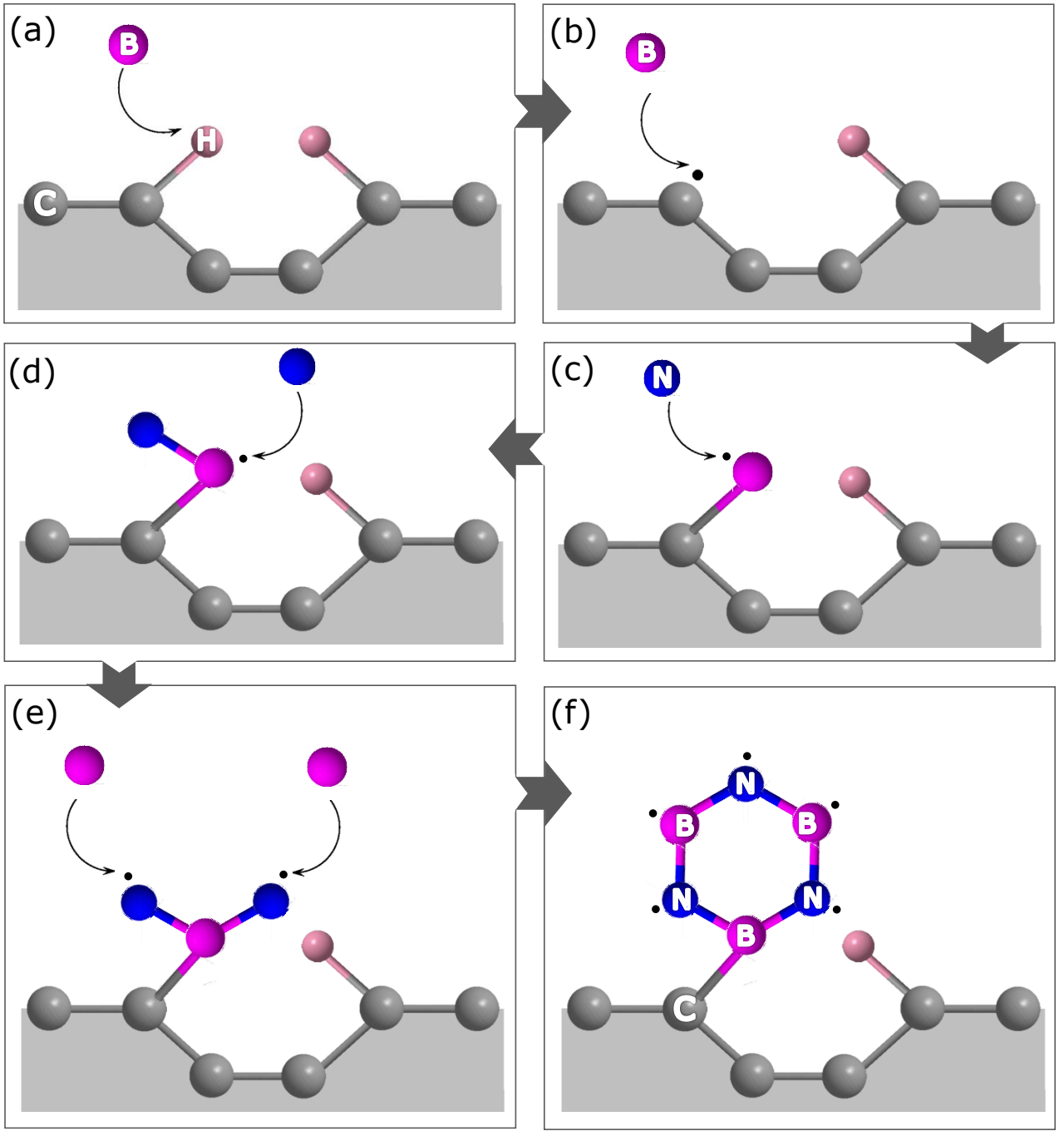


**Figure 7** Schematic illustration of the nucleation of a crystalline hBN nanosheet on a H-terminated diamond surface: (a-b) a sputtered B-ion abstracts and replaces the H-atom at the H-terminated diamond surface; (c-d) sputtered N ions bond to the resulting B sites; (e) sputtered B-ions bond with the resulting N-sites; (f) a sputtered N ion bonds to both of the resulting B sites to form a complete hBN ring, which nucleates the nanosheet.